Prozac® photodegradation mediated by Mn-doped TiO$_2$ nanoparticles: Evaluation of by-products and mechanisms proposal

Ailton J. Moreira [a,b,*], João O.D. Malafatti [a,c], Tania R. Giraldi [b], Elaine C. Paris [c], Ernesto C. Pereira [a], Vagner Romito de Mendonça [d], Valmor Roberto Mastelaro [e], Gian P. G. Freschi [b]

[a] *Chemistry Dept. - Universidade Federal de São Carlos, São Carlos, SP, Brazil*
[b] *Universidade Federal de Alfenas, Campus Poços de Caldas - MG, Brazil*
[c] *Nanotechnology National Laboratory for Agriculture (LNNA), Embrapa Instrumentação, São Carlos, SP, Brazil*
[d] *Federal Institute of Education, Science, and Technology of São Paulo, Itapetininga, SP, Brazil*
[e] *São Carlos Institute of Physics, University of São Paulo, São Carlos, SP, Brazil*

ARTICLE INFO

ABSTRACT

TiO$_2$ nanoparticles were efficiently doped with Mn applying microwave-assisted synthesis method. Anatase phase was confirmed by XRD pattern, which did not exhibit the peaks associated with MnOx contamination. Raman spectroscopy showed a displacement of up to 5 cm^{-1} in the O-Ti-O vibrational mode, suggesting that Ti was replaced by Mn. Oxidation state (Mn^{3+}) was confirmed via high-resolution XPS spectrum of Mn 2p energy level. Incorporation of Mn into the TiO$_2$ network resulted in increased surface area (64.6 m^2 g^{-1}), average particle size up to 16 nm, and bandgap reduction of up to 43 %. The photocatalytic properties of the materials were investigated through Prozac® degradation and improvement of up to 14 % (Ti-0.73 Mn) and 26 % (Ti-0.38 Mn) was seen on comparing doped TiO$_2$ versus pure TiO$_2$ during photocatalysis. Furthermore, after Prozac® photodegradation, TFMP was identified as the main by-product while MAEB and PPMA (other by-products) were seen to compete with each other in the degradation mechanism. In addition to the quantitative analysis done for Prozac®, TFMP, MAEB, and PPMA, LC MS-Q-TOF analysis was performed, confirming that in the presence of Mn-doped TiO$_2$, specific by-products were formed, probably due to more oxidizing species being present in this reaction system. The present study has shown unprecedented evidence that the application of TiO$_2$ nanoparticles efficiently doped with Mn promotes Prozac® degradation by specific mechanisms.

1. Introduction

Charge transport has been one of the most researched properties of nanomaterials in recent years due to its importance to different applications such as electrochemical sensors [1], fuel cells [2], photovoltaic devices [3], and photocatalysts for environmental remediation [4]. In light-irradiated materials, photon absorption promotes the valence electron into the conduction band, giving rise to oxidation (h$^+$) and reduction (e$^-$) sites in their structures [5,6]. However, electron excitation is dependent upon many factors, such as the crystalline structure of the material, bandgap energy, incident photon energy, transport mechanism, and recombination of photogenerated charge carriers [7,8]. Considering that most solar radiation is in the visible region, semiconductors that are able to absorb a wider range of electromagnetic

radiation have broader applications [9,10].

TiO$_2$ is a semiconductor that absorbs UV radiation to promote electronic excitation [11]. When it was modified with dopant elements, its charge transference efficiency and visible light absorption were optimized [9,12–14]. When ZnO, TiO$_2$, or ZrO$_2$ semiconductors were doped with Mn and applied in the photocatalytic degradation of dyes, bandgap reduction was achieved, thereby improving semiconductor performance [15–17]. This is because Mn can be incorporated into the TiO$_2$ network at different oxidation states (2+, 3+, or 4+), distorting its crystalline structure [13,18–20] and optimizing its optical properties. A search of the literature on TiO$_2$ doped with Mn$^{1+ \text{ to } 6+}$ confirmed that the Mn^{4+} dopant had the highest stability [21]. Moreover, Mn^{x+} doping in any TiO$_2$ oxidation state exhibited enhanced photocatalytic properties [21, 22], showing that obtaining materials with reduced bandgap energy

---

may prove to be a potential solution in the control of environmental pollution [23,24]. According to the literature, Mn-doped TiO_2 has been efficiently applied to reduce Cr^{6+} to Cr^{3+} [25], in chemical speciation of metals/non-metals in environmental and food samples [26,27], and in photocatalytic oxidation of emerging contaminants such as pharmaceuticals [28].

To obtain these materials with optimized electronic optical properties, different synthetic routes have been proposed for doping ceramic materials, particularly the microwave-assisted hydrothermal method (MHM) [29,30]. Compared to other synthesis methods, MHM enabled shorter synthesis times, lower processing temperatures and less waste generation [31,32]. Yet, the current methods of choice for obtaining Mn-doped TiO_2 are still the sol-gel method and the hydrothermal method in autoclave [33–36]. Therefore, considering the advantages of MHM and the few reports in the literature for obtaining Mn-doped TiO_2 [37], investigation into this method of synthesis is shown to be promising.

Photoactive materials have been widely applied in the chemical oxidation of environmentally-persistent organic compounds, also denominated emerging contaminants (EC). One of these ECs is fluoxetine, commonly known as Prozac® and used as an antidepressant. Due to the persistence of Prozac® in the environment [38,39], it is an emerging contaminant that has attracted widespread interest in the field of environmental protection and, consequently, has been investigated in advanced oxidation processes [40,41]. Its high consumption has led to the presence of residues in aquatic ecosystems [42] since Prozac® is photochemically stable under visible radiation [43]. However, Prozac® can be oxidized to different intermediates on application of different advanced oxidation processes [41,44]. Literature data have so far only described qualitatively the formation of these intermediates [41,45], limiting progress in the characterization of Prozac®-contaminated ecosystems. One of the Transformation Products (TPs) reported during Prozac® degradation was 4-(Trifluoromethyl)phenol (TFMP) by the following reaction:

Reaction: TFMP formation mechanism after Prozac® degradation [45,46].

Considering that many of these TPs may be formed in different ecosystems, a quantitative approach to this degradation mechanism of Prozac® is deemed urgent and mandatory. In view of the harmful effects Prozac® exerts on aquatic organisms [38,39], quantitative studies of the main TPs formed are scientifically and environmentally relevant. Also, this approach involving both mechanistic and quantitative aspects is of great importance to understanding the influence that different degradation processes have on the Prozac® degradation mechanism and its relationship to the TPs. This work therefore consists of a quantitative investigation of the photodegradation mechanism of Prozac® using Mn-doped TiO_2 photocatalysts obtained by MHM. This degradation mechanism has been quantitatively investigated using high-performance liquid chromatography (HPLC UV) and LCMS-Q-TOF techniques. It must be underlined that three of the by-products formed were defined as major in the degradation mechanism**s** studied since such delineation allows for a better understanding of how Prozac® behaves in the environment. Finally, our results showed that the approach to heterogeneous photocatalysis cannot be restricted to the physical-chemical nature of the material or degradation of the main compound since the by-products formed are also scientifically and environmentally relevant.
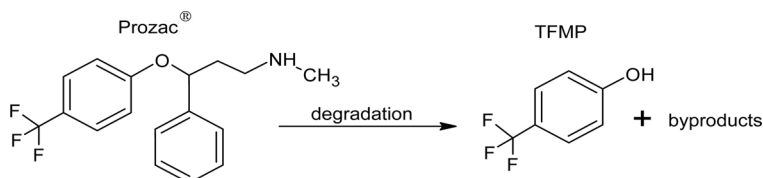
2. Experimental

2.1. Nanoparticle synthesis

For the synthesis of manganese-doped TiO_2 nanoparticles, 12.6 mL of titanium tetraisopropoxide (Sigma-Aldrich) was dispersed in 60 mL of 20 % (v v^{-1}) aqueous isopropanol solution (99 %, Sigma-Aldrich). Manganese acetate tetrahydrate (98 %, Vetec) was added as a source of Mn ions at different molar levels in relation to Ti (Mn/Ti): 0.09, 0.44, 0.87, 2.6, 4.4 mol%. Since isopropanol decreased the dielectric constant of the solution and consequently the microwave heating rate, synthesis was conducted in an alcoholic medium [47].

The mixture was stirred for 1 h under ambient conditions. After the stirring period, the solution was fractionated into 3 portions and transferred to a Teflon® vial (MARSXpress), separately. The reaction system was then subjected to microwave radiation using Mars6 equipment (CEM) applying the three stages of the program: 40 °C, from 0 to 20 min; 60 °C from 21 to 40 min, and 200 °C from 41 to 60 min.

After the heating stage, the samples were washed with methanol (Sigma-Aldrich, centrifuged, and heat-treated (Table 1) in a muffle furnace. The obtained materials were identified as Ti-XMn, where X represents the experimental molar ratio (Mn/Ti) expressed in (%).

2.2. Characterization

The crystalline nature of final powders was analyzed by X-ray diffraction (XRD), using a Shimadzu XRD 6000 diffractometer with a 2θ range from 10° to 70°. Crystallite sizes were estimated by the Scherrer's equation, according to the literature [48]. The chemical bonds type and the crystal lattice disorder degree were identified by Raman spectroscopy, using a Horiba Jobin-Yvon Lab RAM Raman micro-spectrometer equipped with an Olympus TM BX41 microscope. The equipment was operated with an argon laser (λ = 514.5 nm) and a 7 mW source excitation power. The scan was performed in the $77 - 700$ cm^{-1} range with a 5 cm^{-1} resolution. The surface area of the samples was studied by nitrogen physisorption in Micromeritics Gemini VII equipment. About 500 mg of the powder was previously treated at 100 °C under vacuum in a Micromeritics Vap Prep 061 Sample Degas System. The specific surface area was obtained by using the Brunauer-Emmett-Teller (BET) method for a region of $P/P_0 \leq 0.3$. The morphology was characterized by Field Emission Scanning Electron Microscopy (FEG-SEM) (JEOL, JSM-6701 F). Diffuse reflectance UV–vis spectra were obtained using a spectrophotometer LAMBDA 1050 UV/Vis/NIR System with Integrating Sphere, applying the range of 200–800 nm. The concentration of Mn and Ti was determined by Optical Emission Spectroscopy with Inductively Coupled Plasma (ICP-OES), the analytical details being listed in the

Table 1
Heat treatment steps.

Step	Initial/final temperature (° C)	Length of stay at maximum temperature (h)	Heating/cooling rate (°C/min)
1	27 / 200	2	5
2*	27 / 600	2	5

* Before undergoing step 2, the samples were deagglomerated in an agate mortar.

supplementary material.

The chemical analysis of the samples surface was performed by X-ray photoelectron spectroscopy (XPS) using a conventional XPS spectrometer (Scienta Omicron ESCA +) with a 128-channel hemispheric analyzer (EAC2000) with monochrome Al Kα radiation (h ν = 1486.6 eV) as the excitation source. The high-resolution XPS spectra were recorded at a constant pass energy of 20 eV with 0.05 eV per step. During the measurements, a charge neutralizer was used to avoid electrically charging the samples. The XPS spectra were calibrated by the C 1s peak, the binding energy which is located around 284.8 eV. The XPS data were analyzed using the Casa-XPS software.

2.3. Photocatalytic investigation

Standard solutions of Prozac® (98,5%, Santa Cecilia pharmacy), 4-(Trifluoromethyl)phenol (TFMP), α-[2-(Methylamino)ethyl]benzyl-alcohol (MAEB) or (3-phenylpropyl)methylamine (PPMA) (all reagents Sigma-Aldrich with purity > 97 %) 1000 mg L^{-1} were prepared by dissolving the reagents in methanol HPLC grade (JT Backer, USA).

Photolytic experiments in the UV region were performed in a wooden reactor, at 20 °C and 0.94 mW cm^{-2} (254 nm), according described by Moreira et al. [44]. To investigate the influence of initial pH on the photodegradation step, 20 mg L^{-1} Prozac® solutions were prepared with different pH values (2, 5, 7, and 9) using HCl and/or NaOH 0.1 mol L^{-1} to adjustment. Prozac® solutions were subjected to UV photolytic degradation at the different reactions time (from 3 up to 100 min), and after, Prozac®, TFMP, and fluoride concentration was determined.

The photocatalytic essays were conducted by dispersing 10 mg of the semiconductor in 10 mL of the 10.0 mg L^{-1} Prozac® solution. Before irradiation, the samples were subjected to 30 min for the Prozac® adsorption. After this step, under constant stirring, the samples were irradiated at times from 3–120 min. The first sample was collected in 3 min and the other collection intervals were: every 5 min (up to 30 min), every 15 min (up to 60 min), every 30 min (up to 120 min). After each irradiation period, the samples were filtered and analyzed by chromatographic techniques. Here, an HPLC UV/Vis (Agilent 1220 Infinity LC) and a chromatography column Zorbax Eclipse Plus C18 set to 250 × 4.6 mm, 5 μm were used. Under an mobile phase flow rate of 1 mL min^{-1}, and 30 °C temperature, an concentration gradient of formic acid (0.001 % v v^{-1}) (A) / acetonitrile (ACN) was used in the separation, being: 0 min, 95 % (A)/5% (ACN); 0–2 min, 80 % (A)/20 % (ACN); 2–4 min, 50 % (A)/50 % (ACN)/; 4–10 min, 100 % (ACN). The detection was performed at 205 nm and, the figures of merits for the calibration curves were: LOD =0.825 mg L^{-1} / R^2 = 0.999 for Prozac®, LOD =0.348 mg L^{-1} / R^2 = 0.995 for TFMP, LOD =0.387 mg L^{-1} / R^2 = 0.999 for PPMA, and LOD =0.189 mg L^{-1} / R^2 = 0.999 for MAEB. LC–MS QTOF analysis was performed according to the conditions described in a previous study [44].

All measurements were performed in triplicate (n = 3) and the mean standard deviation added in all graphs. Note that due to the sensitivity and precision of the analytic measurements, in some situations the geometric symbols overlap the calculated deviations. Also, calculations of the first-order kinetic constant were performed using the equation ln (C/C$_0$) = kt, with C being the Prozac® concentration at time t, C$_0$ the initial concentration, and t the time in min [44,45]. Kinect constant was calculated for the time interval of up to 30 min since in previous studies it was determined that after this time, the by-products influence the degradation kinetics of Prozac® [44].

For identification of hydroxyl radicals, a probe assay with coumarin (COU) was utilized in this study. According to the literature, COU is hydroxylated in the presence of ˙OH and forms a photoluminescent by-product (umbelliferone), which exhibits emission peak in 452 nm when excited at 332 nm [49,50]. Therefore, 10 mL of COU solution (1.5 mg L^{-1}) was irradiated in the absence and the presence of Ti-0.38 Mn, Ti-0.73 Mn, or Ti-2.8 Mn, using the reactor and conditions,

as described previously. After irradiation and filtration, umbelliferone formation was monitored by molecular fluorescence, using a spectro-fluorophotometer (RF-5301 PC, Shimadzu). Excitation was 332 nm, and emission was monitored at 400–600 nm interval with slit = 5 nm. In addition, an assay was performed by adding 100 μL of ˙OH radical scavenger (DMSO, 98 % Sigma Aldrich) to the reaction system, after which irradiation and photoluminescent analysis were carried out, as described previously.
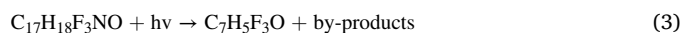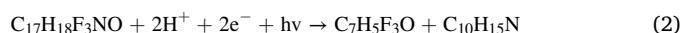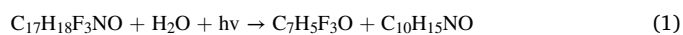
3. Results and discussion

3.1. Photocatalytic degradation of Prozac®

3.1.1. Effect of pH solution

To investigate pH influence, 20 mg L^{-1} Prozac® solution with pH adjusted to different values was submitted to UV irradiation from 3 to 100 min in the absence of a semiconductor and the results were as shown in Fig. 1.

As can be seen in Fig. 1a, Prozac® degradation was over 90 % up to 20 min at different pH values and as Prozac® began to precipitate in the 9–10 pH range [51], we limited our investigation to pH ≤ 9. Thus, the data showed that after TFMP formation reached its maximum in 20 min (Fig. 1b), there was a decrease in Prozac® concentration and almost 100 % removal was achieved upon 40 min of irradiation. However, for the other pH conditions, TFMP presence was significant therefore these results formed the basis for the photodegradation mechanism proposal, illustrated in Fig. 2.

This mechanism suggests that besides TFMP formation, the presence of fluoride in the reaction medium (Fig. 1c) was due to the formation of HF, corroborating the decrease in pH seen in all the conditions studied (Fig. 1d). Therefore, Prozac® photodegradation in the 2–9 pH range does not have a significant influence on the photochemical process and natural conditions (pH ∼ 6.0) may be selected in further studies. Prozac® degradation reactions were represented by Eq.s 1 to 4, by-products were monitored and the influence of materials was evaluated. For clarity, the molecular formulas of the compounds have been shown: Prozac® (C$_{17}$H$_{18}$F$_3$NO), TFMP (C$_7$H$_5$F$_3$O), MAEB (C$_{10}$H$_{15}$NO) and PPMA (C$_{10}$H$_{15}$N)

$$C_{17}H_{18}F_3NO + H_2O + hv \rightarrow C_7H_5F_3O + C_{10}H_{15}NO \qquad (1)$$

$$C_{17}H_{18}F_3NO + 2H^+ + 2e^- + hv \rightarrow C_7H_5F_3O + C_{10}H_{15}N \qquad (2)$$

$$C_{17}H_{18}F_3NO + hv \rightarrow C_7H_5F_3O + \text{by-products} \qquad (3)$$

$$C_{17}H_{18}F_3NO + hv \rightarrow \text{by-products} \qquad (4)$$

3.1.2. Characteristics and effect of substrates

To evaluate substrate effect on the degradation mechanism of Prozac®, TiO$_2$ nanoparticles doped with different Mn concentrations were synthesized. EDX analysis showed that Mn distribution was homogeneous throughout the ceramic material (Fig. S1). Also, real Mn content was quantified using ICP OES and a linear correlation (R^2 = 0.992) was shown between Mn/Ti molar ratio (experimental versus theoretical) (Fig. S2). It can thus be stated that application of the microwave-assisted hydrothermal method was efficient when doping with Mn. In Table 2, it was possible to compare the efficiency of substitutional doping of TiO$_2$ with Mn when different synthesis methods were utilized [13,19,52]. Application of different reagents and synthesis times were also compared. The results showed that the method used in this work not only presented high substitutional doping efficiency, but also shorter synthesis times, and use of fewer reagents. To standardize identification of nanoparticles that had had their Mn/Ti molar ratio experimentally quantified, the following representation will be employed from this point onwards: **Ti-0.00 Mn** (pure TiO$_2$), **Ti-0.11 Mn** (0.11 % Mn),
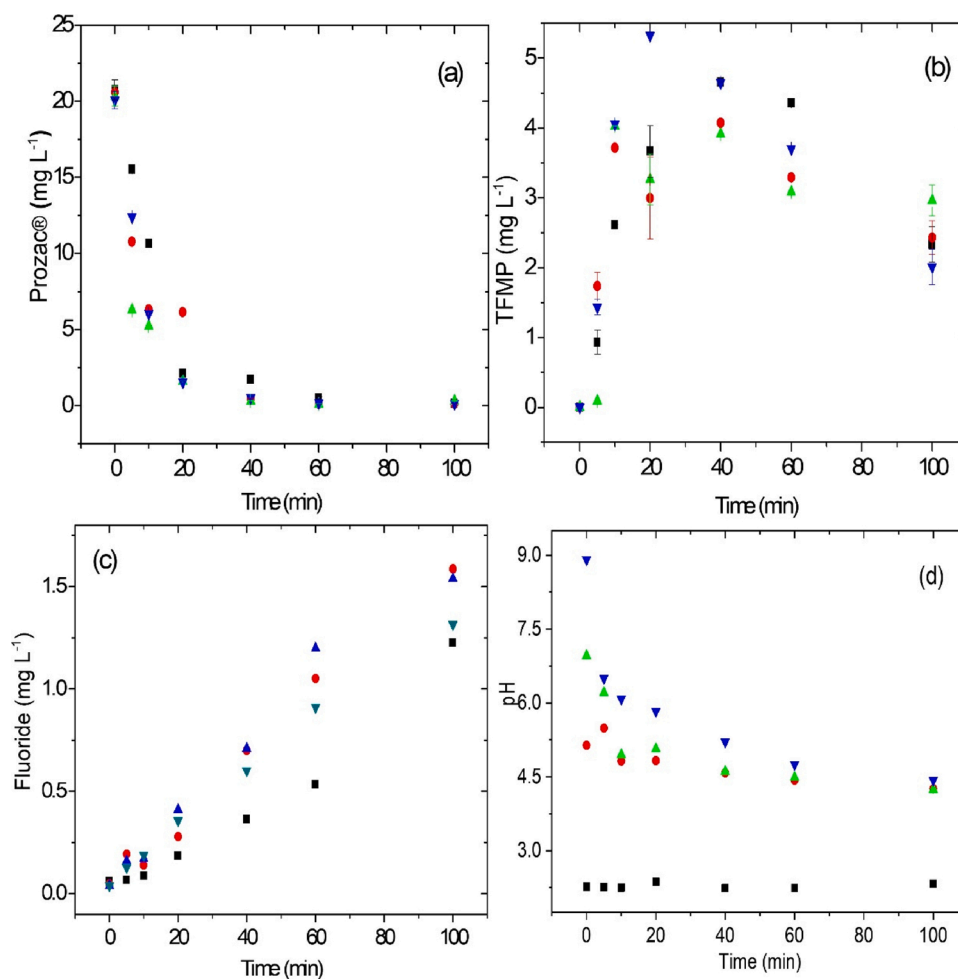
Fig. 1. Influence of initial pH on Prozac® (a) degradation process, TFMP formation (b), fluoride formation (c) and deprotonation (d) after UV irradiation. Being, pH = 2 (■), pH = 5 (●), pH = 7 (▲), pH = 9 (▼).
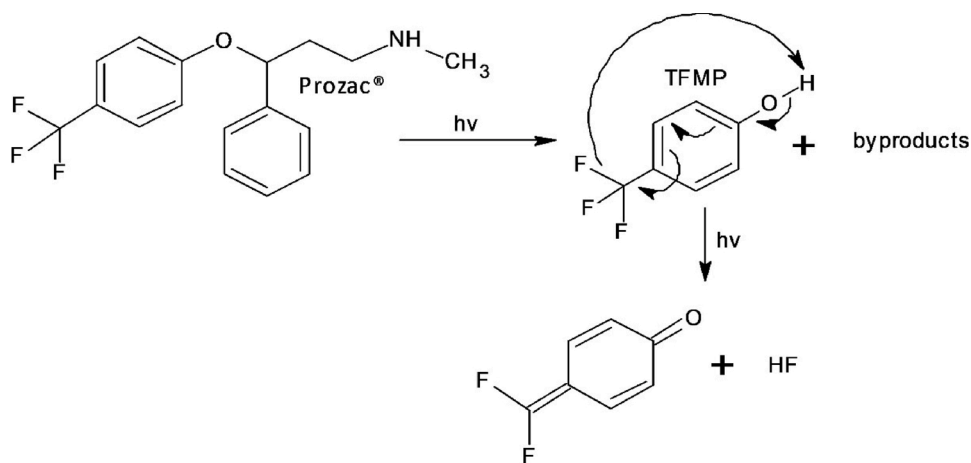

Fig. 2. Possible mechanism of Prozac® photolytic degradation, TFMP formation, dehalogenation and deprotonation.

Ti-0.38 Mn (0.38 % Mn), **Ti-0.73 Mn** (0.73 % Mn), **Ti-1.9 Mn** (1.9 % Mn) and **Ti-2.8 Mn** (2.8 % Mn).
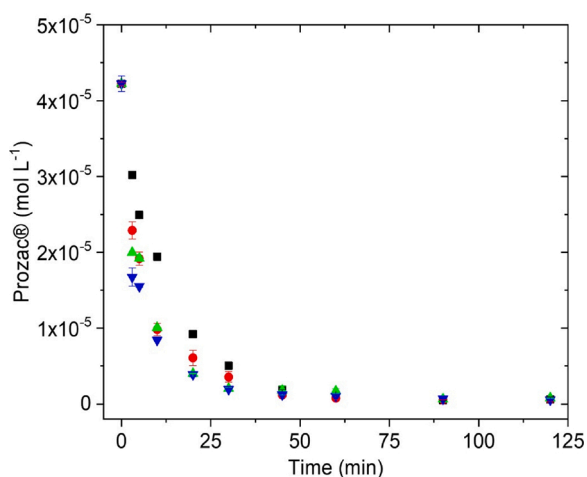
On degrading Prozac® in the absence and presence of different nanomaterials, for the photolytic process, degradation was over 90 % in 40 min, while Ti-0.38 Mn or Ti-0.73 Mn achieved the same removal in 20 min. Herein, the results show that the best performance was obtained from the **Ti-0.38 Mn** and **Ti-0.73 Mn** samples. Note that in Fig. 3 only

the data relative to **Photolysis, Ti-0.00 Mn, Ti-0.38 Mn,** and **Ti-0.73 Mn** were shown, in order to avoid visual confusion; nonetheless, the results for all materials were presented in Fig. S3.

Catalyst influence on different reaction times was compared with the photolytic process during Prozac® degradation. It is important to note that after up to 3 min of irradiation, removal of 28 % (**photolysis**), 46 % (**Ti-0.00 Mn**), 47 % (**Ti-0.11 Mn**), 72 % (**Ti-0.38 Mn**), 60 % (**Ti-**

Table 2

Comparative results of substitutional doping efficiency when different synthesis methods of TiO$_2$ nanoparticles were applied.

Synthesis method/ time (h)	Synthesis reagents	molar% (Mn/Ti)		Quantification Method	Doping efficiency (%)	Reference
		Theoretical	Experimental			
Sol-gel / 29	Tetrabutyl titanate, ethanol, glacial acetic acid, nitric acid, manganese nitrate	3.45	3.14	EDX	91	[19]
Sol-gel / 83	Tetraisopropyl titanate, manganese (II) acetate tetrahydrate, sodium hydroxy, ethanol, hydrochloric acid	4.4	2.5	EDX	57	[52]
Anodization / 10	Titanium foils, acetone, ethanol, ammonium fluoride, phosphoric acid, potassium permanganate	5.1	1.3	XPS	25	[13]
Microwave hydrothermal/ 10	Isopropanol, titanium tetraisopropoxide, manganese (II) acetate tetrahydrate	0.44	0.38	ICP OES	86	This work
		0.87	0.73		84	
		2.6	1.9		73	
		4.4	2.8		64	

Fig. 3. Prozac® concentration variation during degradation process. Photolysis (■), **Ti-0.00 Mn** (●), **Ti-0.38 Mn** (▲), **Ti-0.73 Mn** (▼).

0.73 Mn), 46 % (**Ti-1.9 Mn**), and 41 % (**Ti-2.8 Mn**) was confirmed. This improved performance for the photocatalytic process was expected since the anatase phase of TiO$_2$ was obtained for all materials, as shown in the XRD patterns (Fig. 4a). Moreover, all doped samples exhibited symmetrical peaks and high crystallinity.

XRD peaks indicating the presence of manganese oxides in the doped samples were not observed, and as a result, substitutional doping was suggested. This substitutional mechanism has been reported in previous studies [20] and the doping mechanism justified by the similarity between the ionic radius of Mn$^{4+/3+}$ and that of Ti^{4+}. The TiO$_2$ anatase, rutile, and brookite phases, characterized by diffraction peaks at 2ϴ = 25.4°, 27.5°, and 30.8°, respectively, were identified in all the samples. However, the rutile phase confirmed for **Ti-0.00 Mn** and **Ti-0.11 Mn** had been suppressed with increasing doping while the diffraction peak associated with the brookite phase became more evident (Fig. S4). Crystallinity of the materials, characterized by better-defined peaks in the XRD pattern, decreased as Mn content increased and this was confirmed by decreasing the symmetry of the anatase peaks (37.0°, 37.9°, 38.6°, 54.0°, 55.1°). Since the highest degradation rates for Prozac® occurred in the **Ti-0.38 Mn** and **Ti-0.73 Mn** samples, a further study investigated the influence of Mn on the crystalline properties of the material. To this end, Raman spectroscopy was used to investigate short-range structural changes along the crystal lattice of both pure and doped TiO$_2$. According to Fig. 4b, Raman active modes for anatase were confirmed at 144 cm^{-1} (Eg), 197 cm^{-1} (Eg), 399 cm^{-1} (B1g), 516 cm^{-1} (A1g), and 639 cm^{-1} (Eg). The highest active Eg mode (144 cm^{-1}) corresponds to the symmetrical stretching of the O-Ti-O bonds [37]. As the amount of Mn in the samples was increased, a 5 cm^{-1} decrease in vibration frequency was observed comparing **Ti-0.00 Mn** and **Ti-2.8 Mn**. These results confirmed the symmetry change in TiO$_2$ crystal structure, reinforcing the proposal that Ti^{4+} ions were replaced by the dopant. Also, Raman vibrational mode
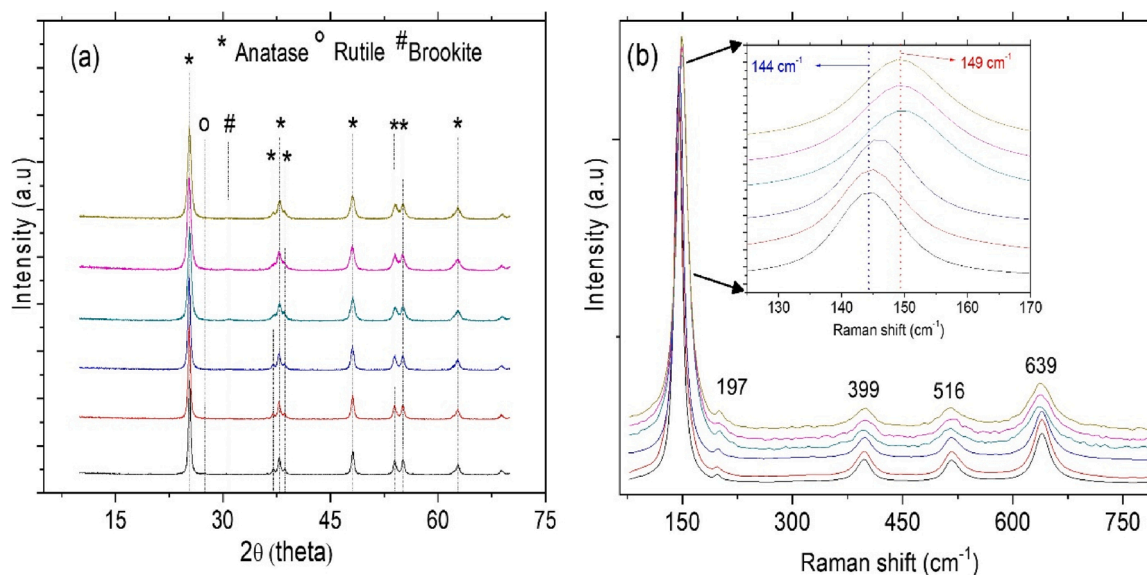
Fig. 4. X-ray diffraction (a) and Raman spectroscopy (b) obtained for the nanomaterials. **Ti-0.00 Mn** (▬), **Ti-0.11 Mn** (▬), **Ti-0.38 Mn** (▬), **Ti-0.73 Mn** (▬), **Ti-1.9 Mn** (▬) and **Ti-2.8 Mn** (▬).

did not reveal Mn-oxide-associated absorption.

X-ray photoelectron spectroscopy (XPS) was used to investigate the surface properties of Ti-0.73Mn, Ti-1.9Mn, and Ti-2.8Mn samples. The XPS high-resolution spectra of O 1s, Ti 2p, and Mn $2p_{3/2}$ is shown in Fig. 5, while Fig. S5 shows the high-resolution XPS spectra of C 1s. Table S1 summarizes the binding energies (eV) of all components studied. The O 1s XPS spectrum peaked at 529.0 and 531.0 eV, which corresponds to the O-(Mn, Ti) lattice oxygen and C—O binding energies, respectively [19,37,53]. The peak at 532.8 eV, according to the literature attributed to O—H bonds or oxygen vacancies, presents higher intensity for the Ti-0.73 Mn sample, indicating that the number of oxygen vacancies in this sample could be higher [53–55]. Adventitious carbon originating either from incomplete Ti (isopropoxide) decomposition or from Mn (acetate) precursors in the heat treatment stages was found in the material according to C 1s binding energy, with peaks exhibited at 285.0 eV (C—O bond) and 287.8 eV (C=O bond) [56]. The XPS spectrum of Ti 2p showed peaks at 458.1 and 464.0 eV, which were attributed to Ti $2p_{3/2}$ and Ti $2p_{1/2}$ levels, respectively, confirming the presence of Ti^{4+}, as reported in the literature [19,20]. Additionally, the difference between the two energy levels was approximately 6.0 eV and a near-471.0 eV satellite peak is characteristic of TiO_2 compounds [19]. XPS spectra showed that the peak intensity attributed to levels Mn $2p_{3/2}$ and Mn $2p_{1/2}$ was easily measured in Ti-1.9 Mn (Fig. 5f) and Ti-2.8 Mn samples (Fig. 5i), but at noise level for the Ti-0.73 Mn sample (Fig. 5c) due to its low dopant content. However, Mn doping in all samples was confirmed by quantitative analysis using ICP OES. The XPS spectrum of Mn 2p exhibited peaks at 641.4 and 653.5 eV, which were attributed to the Mn $2p_{3/2}$ and Mn $2p_{1/2}$ levels, respectively, a finding that bears out the presence of Mn^{3+} [13,19].

After confirming deformation in the crystalline lattice of the samples doped with Mn^{3+} using diffuse reflectance analysis, we investigated how the presence of Mn affects light absorption (Fig. S6). While visible (500 nm) absorption was 25 % for **Ti-0.00 Mn**, by increasing Mn in the semiconductor, absorption values also increased, to the order of 45, 60, 69, 70, and 76 % from **Ti-0.11 Mn** up to **Ti-2.8 Mn**, respectively. This change corresponded to an increase of up to 51 % in the visible spectrum absorption rate for **Ti-2.8 Mn** compared to **Ti-0.00 Mn**. Bandgap values, calculated using the Kubelka–Munk (K—M) function, are shown in Table 3.

Bandgap results (Table 3) showed that if the amount of dopant is increased, the energy required for electronic transition is reduced by up to 43 %, thereby improving its photocatalytic activity. Thus, the physical properties of nanomaterials were examined against first-order kinetic constant (k = min^{-1}), which was calculated according to parameters in the existing literature [44,45]. It is worthy of note that in this step, the photocatalytic assays were performed under UV light since, according to Yin et al. [43], Prozac® is highly stable under visible light. Thus, considering that the central focus of this study was to assess semiconductor influence on the Prozac® degradation mechanism, only UV light was able to provide the necessary by-products for the comparative discussion. Therefore, in this work, these materials were not applied in the visible region.
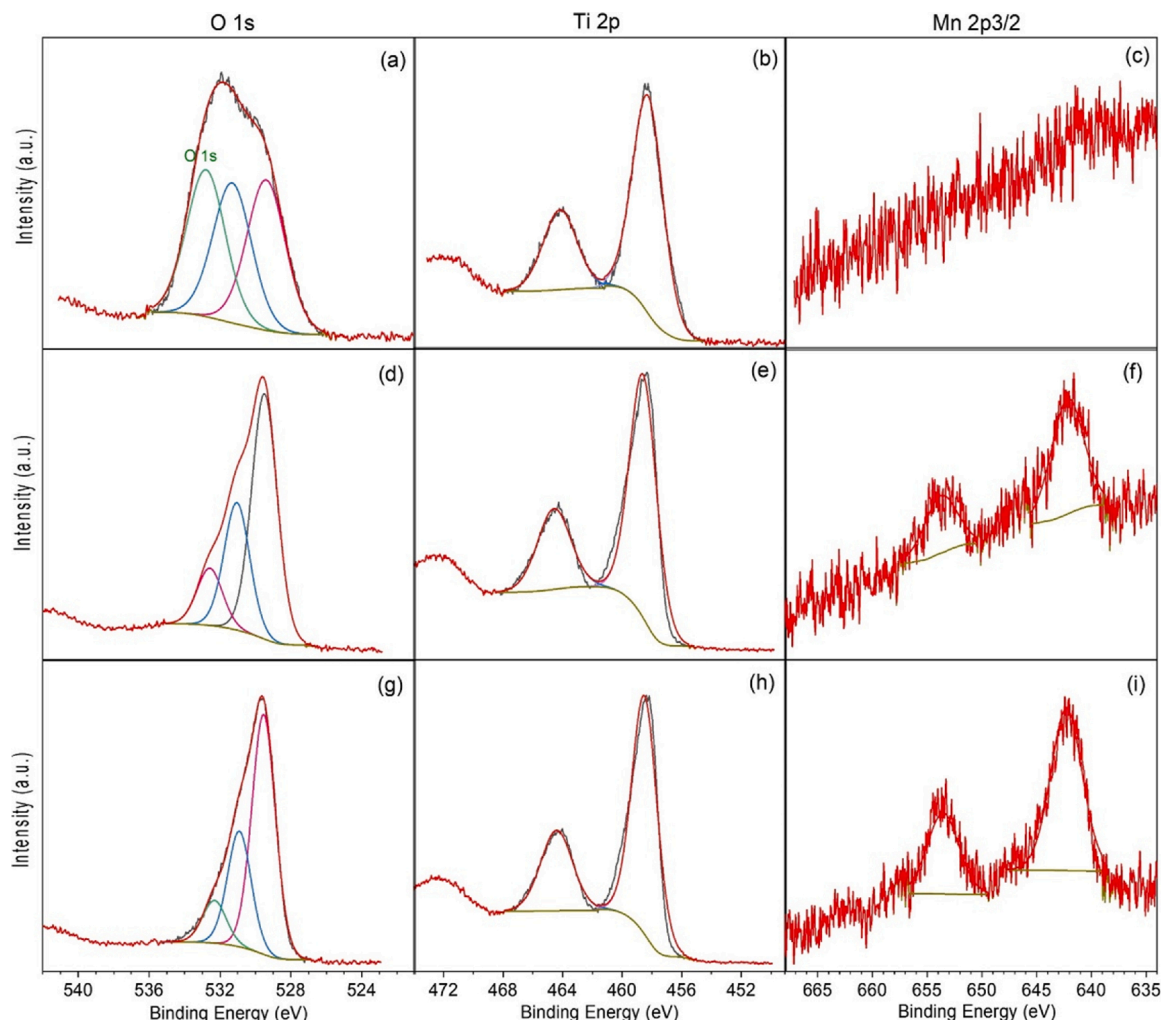

Fig. 5. XPS spectra of O 1s, Ti 2p, or Mn 2p of the Ti-0.73Mn (a, b, c) T-1.9Mn (d, e, f), and Ti-2.8Mn (g, h, i) samples.

Table 3
Characteristics of doped and undoped nanoparticles.

Sample	k x 10^{-2} (min^{-1}) / R^2	Band gap (eV)	BET surface area ($m^2\,g^{-1}$)	Crystallite size (nm)
Photolysis	6.62 ± 0.21 / 0.996	–	–	–
Ti-0.00 Mn	6.76 ± 0.22 / 0.948	2.88	30.5	24
Ti-0.11 Mn	5.97 ± 0.19 / 0.995	2.77	31.0	21
Ti-0.38 Mn	8.80 ± 0.28 / 0.981	2.29	36.1	20
Ti-0.73 Mn	8.14 ± 0.26 / 0.980	2.10	49.2	15
Ti-1.9 Mn	6.99 ± 0.22 / 0.888	2.00	64.6	13
Ti-2.8 Mn	6.53 ± 0.20 / 0.837	1.65	47.6	15

First-order kinetic constants were 25 and 23 % higher for **Ti-0.38 Mn** compared to photolysis and photocatalysis with **Ti-0.00 Mn**, respectively. Likewise, k showed an increase of up to 19 and 17 % for **Ti-0.73 Mn** when compared to photolysis and photocatalysis with **Ti-0.00 Mn**, respectively. These results were in accordance with the larger surface areas observed for **Ti-0.38 Mn** and **Ti-0.73 Mn,** and corroborated the reduced bandgap values found for these samples (Table 3). The Mn-doped samples displayed larger surface areas compared to the undoped ones which suggested that the addition of Mn had inhibited grain growth and had promoted this increment. Thus, larger surface

areas in the doped samples may be associated to the smaller atomic radius of substitutional Mn^{3+} whose presence on the ceramic network wasconfirmed by XPS analysis. According to the literature, when an Mn^{3+} ion replaces a Ti^{4+} ion, there is a decrease in cell volume [17] that results in a decrease in particle size and consequent increase in BET surface area.

Fig. 6 confirmed that mean particle size decreased as dopant concentration increased, on a range from 28 ± 5 nm (**Ti-0.00 Mn**) to 16 ± 2 nm (**Ti-2.8 Mn**). These data were also supported by surface area results and crystallite sizes calculated by Scherrer Equation (Table 3), demonstrating that each particle was indeed a crystallite. Further, a noticeable trend was observed in which BET surface area tended to increase and crystallite/particle size to decrease as larger amounts of dopant (up to 1.9 % mol) were added. With respect to the only material that does not follow this trend (**Ti-2.8 Mn**), it is important to take into account that doping efficiency was calculated at 63 %, which represented the lowest value among all the doped materials.

As photocatalytic performance improved for Ti-0.38 Mn and Ti-0.73 Mn, hydroxyl radical ($^\cdot$OH) formation was investigated. Photoluminescence spectra showed peaks centered at 452 nm for Ti-0.38 Mn and Ti-0.73 Mn, confirming umbelliferone formation (Fig. S7a). These assays were also performed for the photolytic process and Ti-2.8 Mn. However, no peak was shown for the photolytic process (as expected) and Ti-2.8 Mn, indicating that in this material with reduced bandgap, recombination processes had inhibited $^\cdot$OH formation at levels undetectable by PL. Thus, improved photoactivity for Ti-0.38 Mn and Ti-0.73 Mn showed greater efficiency in producing the oxidizing species
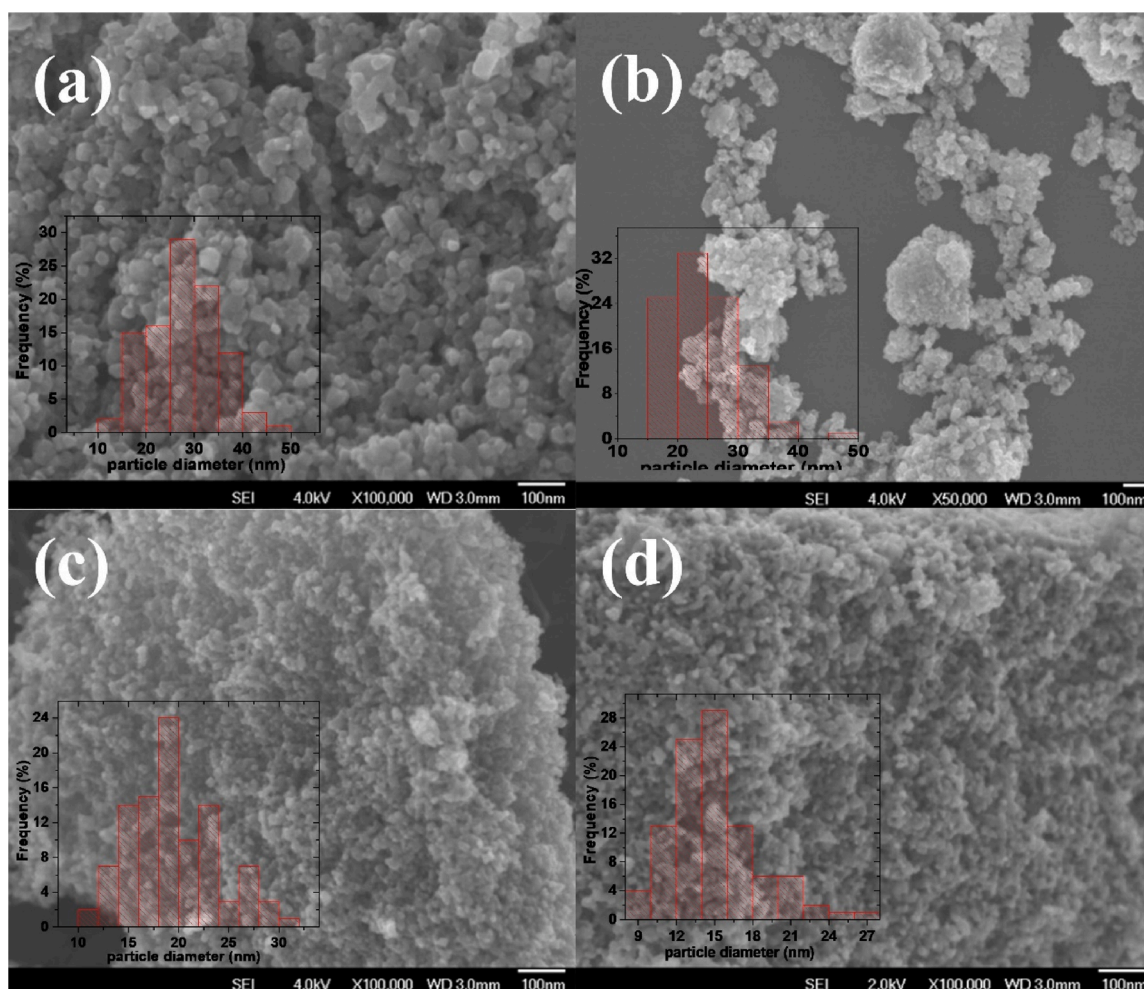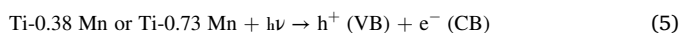

Fig. 6. FEG-SEM images and their respective particle mean diameter measurements (a) **Ti-0.00 Mn**, (b) **Ti-0.11 Mn**, (c) **Ti-0.73 Mn** and (d) **Ti-2.8 Mn.**

($^{\bullet}$OH), responsible for reacting with COU ($C_9H_6O_2$) and forming umbelliferone ($C_9H_6O_3$), according to Eqs. 5 to 8. As reported in the literature, COU is also converted to other species during chemical oxidation [49,57]. Thus, when a photogenerated electron is abstracted on the catalyst surface by molecular O_2, superoxide radicals ($^{\bullet}O_2^-$) are produced, as shown in Eq. 8 [58]. The high reactivity of $^{\bullet}O_2^-$ then promotes COU oxidation in other byproducts (Eq. 9), thus completing the photocatalytic mechanism. Furthermore, these suggested $^{\bullet}O_2^-$ may be responsible for forming the Prozac® oxidation by-products shown in Eqs. 3 or 4.

$$\text{Ti-0.38 Mn or Ti-0.73 Mn} + h\nu \rightarrow h^+ \text{ (VB)} + e^- \text{ (CB)} \quad (5)$$

$$H_2O + h^+ \text{ (VB)} \rightarrow {}^{\bullet}OH + H^+ \quad (6)$$

$${}^{\bullet}OH + C_9H_6O_2 \rightarrow C_9H_6O_3 + H^+ \quad (7)$$

$$e^- \text{ (CB)} + O_2 \rightarrow {}^{\bullet}O_2^- \quad (8)$$

$$C_9H_6O_2 + {}^{\bullet}O_2^- + 2H^+ \rightarrow \text{byproducts} \quad (9)$$

Hydroxyl radical production in the presence of Ti-0.38 Mn and Ti-0.73 Mn corroborate the optimized physicochemical properties of these materials, such as high doping efficiency, reduced bandgap, and high surface area. In order to fully elucidate the formation of $^{\bullet}$OH, Fig.S7b shows that the peaks centered at 452 nm were absent in the added DMSO solutions which act as a hydroxyl radical scavenger [40,59]. With increased irradiation time, Prozac® removal attained 88 % (**photolysis**) and 95 % (**Ti-0.73 Mn**) after 30 min. It is important to point out here that the literature does not have many studies associated with the photocatalytic degradation of Prozac® and the quantitative monitoring of its by-products. Nonetheless, Table 4 shows the few reports found for Prozac® degradation [60–62] allowing for comparison with the synthesized materials applied in this study.

3.1.3. Main transformation products

Prozac® degradation was always accompanied by the formation of TFMP, MAEB, and PPMA (Fig. 7).

According to Eq.s 1,2, and 3, TFMP byproduct was present in more than one degradation mechanism pathway (Eqs. 1,2 and 3), while PPMA and MAEB were each suggested in only one mechanism (Eq. 1 and 2, respectively). Therefore, TFMP molar concentration was expected to be higher than the concentrations of MAEB and PPMA. On the other hand, in the Prozac® degradation mechanism, MAEB and PPMA proceeded along different paths and their molar concentrations (formation) were expected to be inversely proportional, that is, if one increased the other would decrease. The quantitative data obtained in our study confirmed that TFMP concentration reached values 3.6 ± 0.11 times higher than the concentrations determined for MAEB and PPMA. This unexpectedly high concentration could be justified by the fact that the concentrations of MAEB and PPMA decrease after 20 min, while that of TFMP begins to

decrease after 40 min. Such behavior indicated that TFMP was less susceptible to photocatalytic degradation than MAEB and PPMA. We also found that the PPMA / MAEB molar ratio reached 0.9, indicating that the formation mechanism of these by-products does not have a preferential route in the photolytic process for the evaluated time (30 min). For clarity purposes, Table 5 shows maximum conversion rates (μmol L^{-1} min^{-1}) of Prozac® in MAEB, PPMA, and TFMP. These rates were calculated by determination of the ratio using the highest molar concentration formed by the TP over its respective time period, expressed in min.

Maximum conversion rates to TFMP were approximately 2 times higher than those calculated for MAEB and PPMA in the photocatalytic process, reinforcing the mechanisms described by Eqs. 1 and 2. It is noteworthy that the maximum conversion rates were influenced by the secondary degradation mechanisms since MAEB, PPMA, and TFMP by-products were also degraded in the process, as depicted in Fig. 7. Thus, PPMA and TFMP degradation were greater for photocatalysis applying **Ti-0.38 Mn** and **Ti-0.73 Mn**. This finding suggests that the degradation of these by-products cannot be neglected from the very moment they are first formed. Therefore, it is correct to state that these by-products compete with Prozac® in the degradation process, which justifies the low linear correlation of the kinetic constant calculated for **Ti-1.9 Mn** and **Ti-2.8 Mn**. All the same, this influence was more significant after 30 min of process. In order to clearly certify no other Prozac® degradation by-products besides MAEB, PPMA, and TFMP were present, we performed an HPLC/MS Q-TOF analysis of samples degraded with **Ti-2.8 Mn** at 3 and 60 min.

3.1.4. Degradation mechanism of Prozac®

Photocatalytic degradation efficiency was higher for **Ti-0.73 Mn** samples (Fig. 3), and the number of TPs formed was equal for all doped materials. However, for mass spectrometric identification of the compounds, samples with higher peaks were selected so as to improve detection. Therefore, an aliquot of the photodegraded samples in the presence of **Ti-2.8 Mn** was subjected to HPLC MS Q-TOF analysis. Fig.S8 shows the chromatograms obtained after photocatalytic degradation at 3 min or 60 min which identified 17 TPs formed from Prozac® degradation. At 3 min degradation, 8 peaks were identified (Fig.S8a) and, at 60 min degradation, a significant decrease in TP12 (Prozac®) was confirmed. At the same time, TP6 and TP14 increased, and a new TP was formed (Fig. S8b). These results therefore bear out the hypothesis that the amount of TP formed early in the Prozac® degradation process is not restricted to MAEB, PPMA, and TFMP (quantified in this study), thus confirming Eqs. 3 and 4.

After mass spectra identification (Table 6), proposed mechanisms for Prozac® degradation were shown (Fig. 8). In **Mechanism 1**, trihalogenated carbon (TP12) goes through a hydroxylation process, forming a carboxylic acid group (TP6). As the process progresses, TP6 undergoes gradual hydroxylation and/or de-alkylation processes, forming structures with a higher number of hydroxyls, and absent from the methyl group initially bound to aminic nitrogen (TP5, TP7, TP10, TP11, TP13 e TP16). **Mechanisms 2** and **5** were both direct and simple since only one compound was formed by each route. Even so, for **Mechanisms 2** and **5**, the process of hydroxylation was present, as well as those of de-alkylation and de-amination, the latter confirmed by the presence of TP14. **Mechanism 3** confirmed Eq. 1 wherein MAEB and TFMP were formed after breaking the ether bond in TP12 by a radical attack. Finally, **Mechanism 4** has a high number of hydroxylated structures which suggests the likelihood of a radical hydroxylation mechanism, corroborating the results that proved $^{\bullet}$OH formation (Fig. S7). It is important to highlight that TP8, TP10, TP11, and TP13 were obtained exclusively when Prozac® was degraded by application of Mn-doped TiO_2, reinforcing the influence of the material on the degradation mechanism.

Table 6 shows structure suggestions for the different TPs that integrate the degradation mechanism referred to in Fig. 8. These molecules
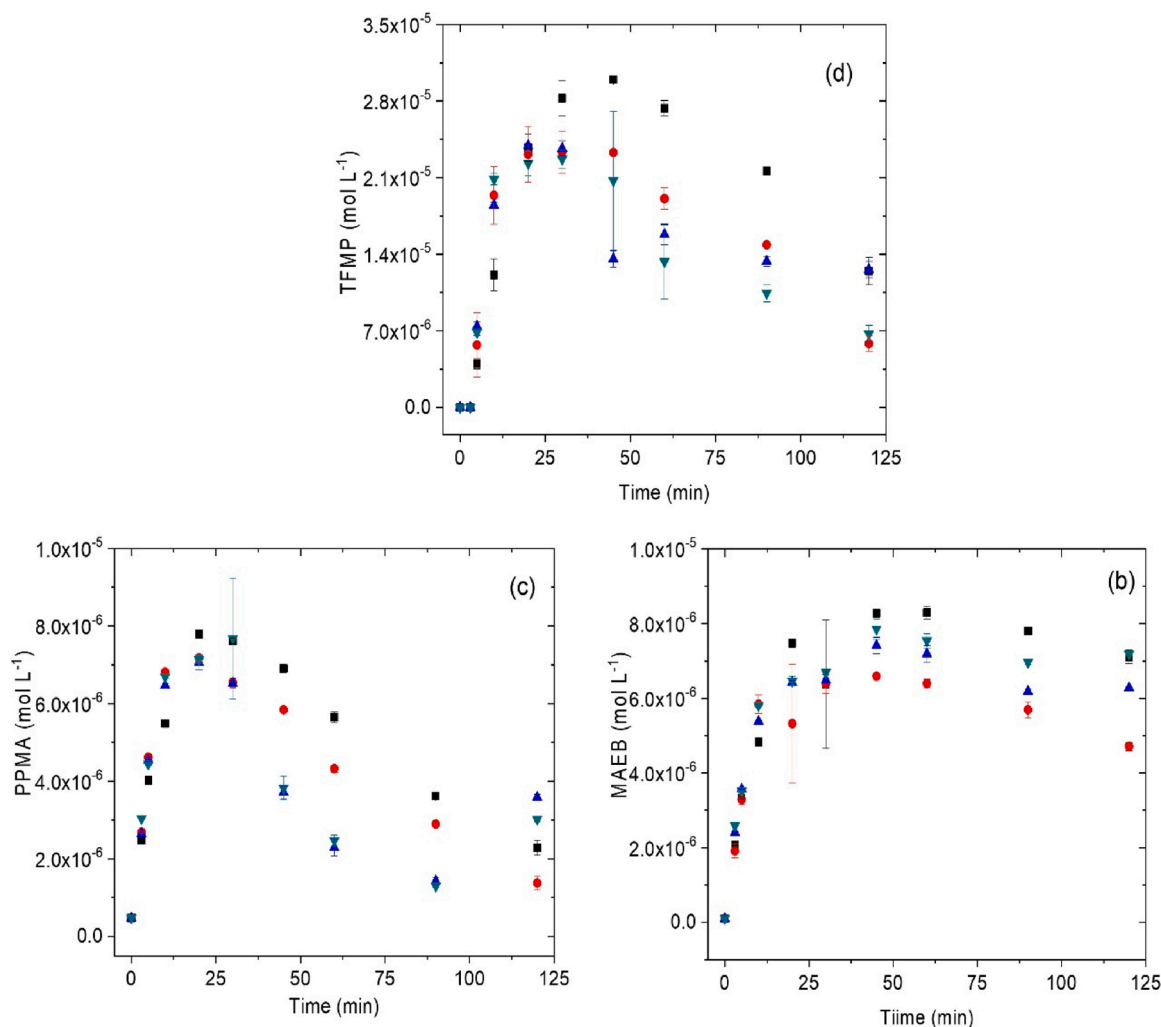
Table 4
Comparative results of Prozac® degradation through photocatalytic processes.

Material / suspension (g L^{-1})	Prozac® mg L^{-1} *	Prozac® degradation (%) / time (h)	k x 10^{-2} (min^{-1})	monitored by-products?	Reference
TiO_2(P25) / 0.7	20	21 / 1	0.39		
TiZnSiO$_2$ / 0.7	20	21 / 1	0.39	no	[60]
TiO_2 / 1	0.2	90 / 0.5	**		[61]
HAPTi / 4	8	80 / 25	0.13		[62]
Ti-0.00 Mn / 1	10	91 / 0.5	6.8	yes	
Ti-2.8Mn / 1		95 / 0.5	8.1		This work

* initial concentration of Prozac®.
** not available.

Fig. 7. TFMP (a), PPMA(b) and MAEB(c) concentration variation during degradation process. **Photolysis** (■), **Ti-0.00 Mn** (●), **Ti-0.38 Mn** (▲), **Ti-0.73 Mn** (▼).

Table 5
Conversion maximum of Prozac® into MAEB, PPMA and TFMP, expressed in $\mu mol\ L^{-1}\ min^{-1}$ after photocatalytic degradation.

Process	Convertion maximium rates ($\mu mol\ L^{-1}\ min^{-1}$)		
	Prozac®→MAEB	Prozac®→PPMA	Prozac®→TFMP
Photolysis	0.69	0.83	1.21
Ti-0.00 Mn	0.66	0.90	1.94
Ti-0.11 Mn	0.51	0.68	1.21
Ti-0.38 Mn	0.80	0.91	1.85
Ti-0.73 Mn	0.86	1.01	2.08
Ti-1.9 Mn	0.77	0.89	1.95
Ti-2.8 Mn	0.46	0.56	1.02

were suggested after interpretation of their respective mass spectra (m / z [H+]), calculated mass, elemental composition, and relative error, obtained by the MassHunter software.

4. Conclusions

In the present study, Mn-doped TiO_2 nanoparticles were obtained by the microwave-assisted hydrothermal method. Using only 3 reagent types and microwave irradiation time of only 1 h, it was possible to achieve $\geq$ 64 % doping efficiency. Substitutional doping of TiO_2 by Mn^{3+} was confirmed using Raman spectroscopy, XRD, ICP OES elemental analysis, and XPS analysis. Increased doping resulted in
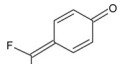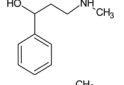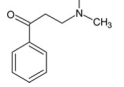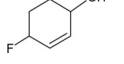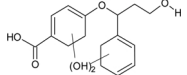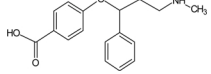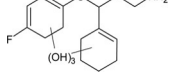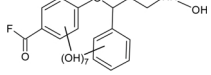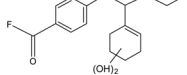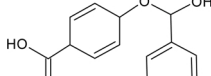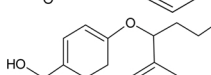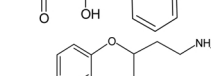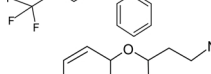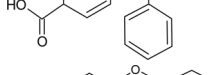
smaller particle sizes (16 nm) and increased BET surface area (up to 64.6 $m^2\ g^{-1}$). It was also confirmed that the dopant enhanced the capacity of the material to absorb electromagnetic radiation in the UV–vis region, thus broadening the range of its potential applications. When Ti-0.38 Mn was applied in the photocatalytic degradation process of Prozac® under UV radiation in 3 min, a 44 % in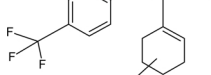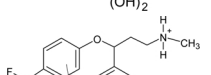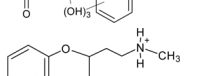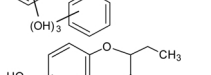crease in efficiency was confirmed. First-order kinetic constant also showed an increase of up to 25 %, indicating Ti-0.38 Mn had performed best. Prozac® degradation mechanisms for MAEB, TFMP, and PPMA were quantitatively discussed, whilst 16 by-products were identified on qualitative analysis. Through this combined quali-quantitative approach it was possible to correlate the influence of the different materials on Prozac® degradation and on TP formation/degradation. The data gathered herein may prove valuable for future studies seeking to better understand the behavior of Prozac® and its TPs in different aquatic ecosystems.

CRediT authorship contribution statement

Ailton J. Moreira: Investigation, Writing - review & editing. **João O. D. Malafatti:** Investigation. **Tania R. Giraldi:** Writing - review & editing, Validation. **Elaine C. Paris:** Writing - review & editing, Validation. **Ernesto C. Pereira:** Writing - review & editing. **Vagner Romito de Mendonça:** Writing - review & editing, Validation. **Valmor Roberto Mastelaro:** Investigation, Writing - review & editing. **Gian P.G. Freschi:** Conceptualization, Resources, Writing - review & editing.

Table 6
TP identified by HPLC-MS/Q-TOF after photocatalytic degradation of Prozac®.

Transformation Product	t_r (min)	(m/z) [H$^+$]	Elemental composition	Calculated mass	Error (ppm)	Molecular structure (Suggestion)
TP1	0.26	143.0037	$C_7H_4F_2O$	142.0229	*	
TP2	0.36	166.1253	$C_{10}H_{15}NO$	165.1180	−15.85	
TP3	0.81	178.1250	$C_{11}H_{15}NO$	177.1177	−13.23	
TP4	1.05	117.0731	C_6H_9FO	116.0657	−17.22	
TP5	2.45	310.1427	$C_{16}H_{21}O_6$	309.1355	−5.39	
TP6	2.55	286.1452	$C_{17}H_{19}NO_3$	285.1379	−5.01	
TP7	3.65	300.1607	$C_{15}H_{22}FNO_4$	299.1534	−0.47	
TP8	4.3	402.0838	$C_{16}H_{16}FNO_{10}$	401.0761	−0.57	
TP9	4.70	310.1429	$C_{16}H_{20}FNO_4$	309.1357	6.39	
TP10	5.02	246.2446	$C_{14}H_{14}O_4$	246.2586	*	
TP11	5.16	290.2698	$C_{16}H_{19}NO_4$	289.3264	*	
TP12	5.33	310.1425	$C_{17}H_{18}F_3NO$	309.1353	−4	
TP13	6.21	274.2755	$C_{16}H_{19}NO_3$	273.3270	*	
TP14	6.32	317.1373	$C_{16}H_{19}F_3O_3$	316.1301	−4.6	
TP15	6.94	337.2362	$C_{17}H_{20}FNO_5$	336.2283	*	
TP16	7.44	291.2541	$C_{16}H_{20}NO_4$	290.3337	*	
TP17	8.11	305.2731	$C_{16}H_{16}O_6$	304.2652	*	
TP18 **	–	161.0221 (-ESI)	$C_7H_5F_3O$	162.0293	−0.54	

* The suggested elemental composition for the TP are not followed by the MassHanter Aquisition Data software.
** The compound is only detected in the ESI(-) mode, and thus, its retention time (t_r) is not being reported.
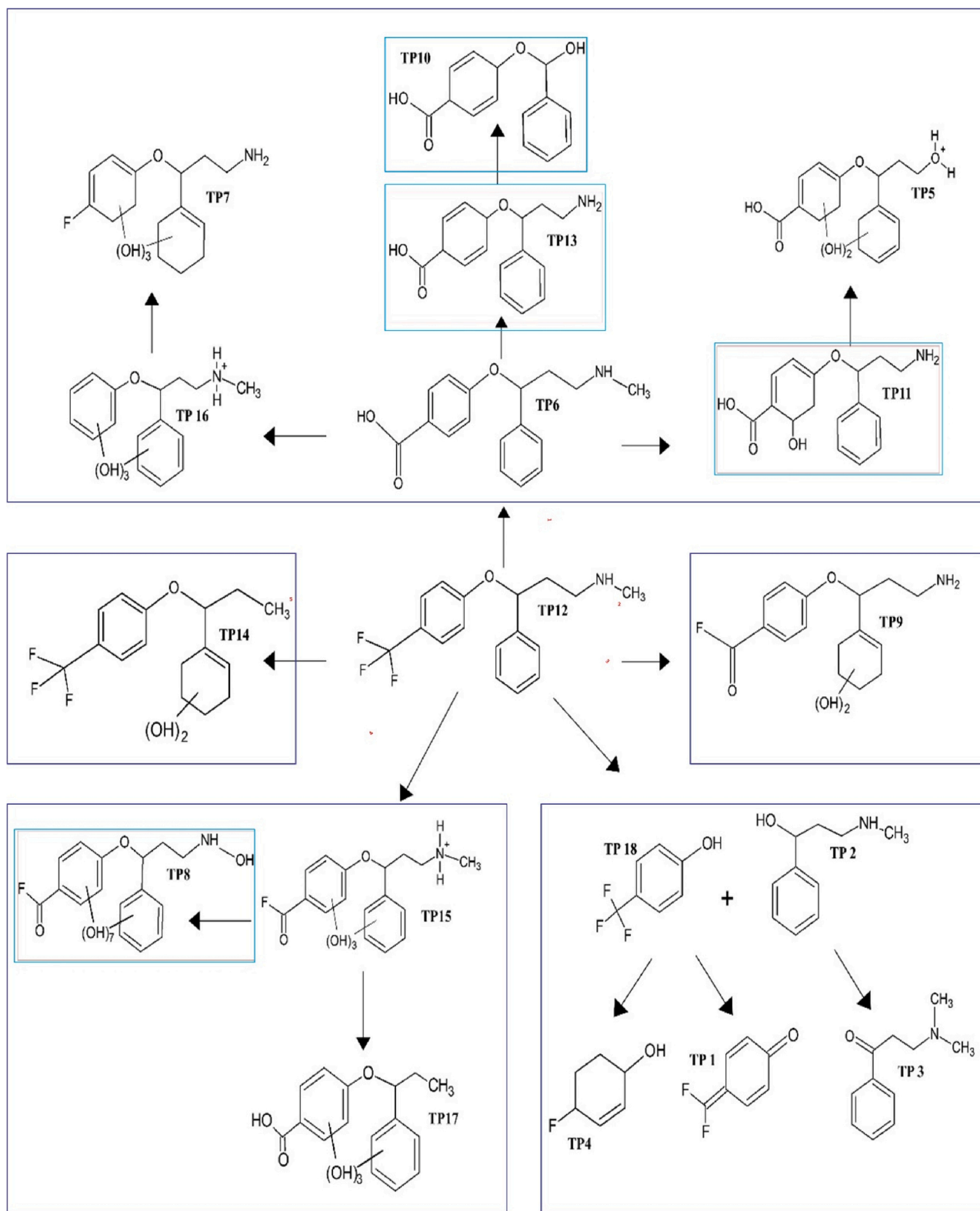
Fig. 8. Suggestion of photocatalytic degradation mechanism of Prozac® after identification by HPLC-MS-Q-TOF. **Note:** Prozac® (TP12), MAEB (TP2), TFMP (TP18). Blue-demarcated molecules were observed only for photocatalysis in the presence of Mn-doped TiO_2.

Declaration of Competing Interest

The authors report no declarations of interest.

Acknowledgments

de Nível Superior (CAPES – grant # 88887.368533/2019-00 and Code # 001) and CNPq (Proc. 444117/2014-8), SisNano/MCTIC is gratefully acknowledged.

Appendix A. Supplementary data

Supplementary material related to this article can be found, in the online version, at doi:https://doi.org/10.1016/j.jece.2020.104543.

References

[1] R. Suresh, K. Giribabu, R. Manigandan, S.P. Kumar, S. Munusamy, S. Muthamizh, A. Stephen, V. Narayanan, New electrochemical sensor based on Ni-doped V 2 O 5 nanoplates modified glassy carbon electrode for selective determination of dopamine at nanomolar level, Sens. Actuators, B Chem. 202 (2014) 440–447, https://doi.org/10.1016/j.snb.2014.05.095.

[2] Y. Ye, H. Bruning, X. Li, D. Yntema, H.H.M. Rijnaarts, Significant enhancement of micropollutant photocatalytic degradation using a TiO 2 nanotube array photoanode based photocatalytic fuel cell, Chem. Eng. J. 354 (2018) 553–562, https://doi.org/10.1016/j.cej.2018.08.064.

[3] A. Mashreghi, F. Davoudi, The effect of ethylene glycol/citric acid molar ratio in the initial precursor of TiO2 nanoparticle paste synthesized by a polymerizable complex method on the photovoltaic properties of dye-sensitized solar cells, Mater. Sci. Semicond. Process. 30 (2015) 618–624, https://doi.org/10.1016/j.mssp.2014.11.001.

[4] O.F. Lopes, E.C. Paris, C. Ribeiro, Synthesis of Nb2O5 nanoparticles through the oxidant peroxide method applied to organic pollutant photodegradation: a mechanistic study, Appl. Catal. B Environ. 144 (2014) 800–808, https://doi.org/10.1016/j.apcatb.2013.08.031.

[5] R. López, R. Gómez, Band-gap energy estimation from diffuse reflectance measurements on sol-gel and commercial TiO 2: a comparative study, J. Solgel Sci. Technol. 61 (2012) 1–7, https://doi.org/10.1007/s10971-011-2582-9.

[6] M. Hassan, Y. Zhao, B. Xie, Employing TiO2 photocatalysis to deal with landfill leachate: current status and development, Chem. Eng. J. 285 (2016) 264–275, https://doi.org/10.1016/j.cej.2015.09.093.

[7] E. Jimenez-Relinque, M. Castellote, Hydroxyl radical and free and shallowly trapped electron generation and electron/hole recombination rates in TiO 2 photocatalysis using different combinations of anatase and rutile, Appl. Catal. A Gen. 565 (2018) 20–25, https://doi.org/10.1016/j.apcata.2018.07.045.

[8] Z.-H. Cui, F. Wu, H. Jiang, First-principles study of relative stability of rutile and anatase TiO 2 using the random phase approximation, Phys. Chem. Chem. Phys. 18 (2016) 29914–29922, https://doi.org/10.1039/c6cp04973g.

[9] Y. Chen, W. Li, J. Wang, Y. Gan, L. Liu, M. Ju, Microwave-assisted ionic liquid synthesis of Ti3+ self-doped TiO2 hollow nanocrystals with enhanced visible-light photoactivity, Appl. Catal. B Environ. 191 (2016) 94–105, https://doi.org/10.1016/j.apcatb.2016.03.021.

[10] M. Humayun, F. Raziq, A. Khan, W. Luo, Modification strategies of TiO 2 for potential applications in photocatalysis: a critical review, Green Chem. Lett. Rev. 11 (2018) 86–102, https://doi.org/10.1080/17518253.2018.1440324.

[11] D. Dambournet, I. Belharouak, K. Amine, Tailored preparation methods of TiO2 anatase, rutile, brookite: mechanism of formation and electrochemical properties, Chem. Mater. 22 (2010) 1173–1179, https://doi.org/10.1021/cm902613h.

[12] M. Stucchi, C.L. Bianchi, C. Pirola, S. Vitali, G. Cerrato, S. Morandi, C. Argirusis, G. Sourkouni, P.M. Sakkas, V. Capucci, Surface decoration of commercial micro-sized TiO2 by means of high energy ultrasound: a way to enhance its photocatalytic activity under visible light, Appl. Catal. B Environ. 178 (2014) 124–132, https://doi.org/10.1016/j.apcatb.2014.10.004.

[13] Z. Xu, C. Li, N. Fu, W. Li, G. Zhang, Facile synthesis of Mn-doped TiO2 nanotubes with enhanced visible light photocatalytic activity, J. Appl. Electrochem. 48 (2018) 1197–1203, https://doi.org/10.1007/s10800-018-1198-y.

[14] W.F. Chen, S.S. Mofarah, D.A.H. Hanaor, P. Koshy, H.K. Chen, Y. Jiang, C. C. Sorrell, Enhancement of Ce/Cr codopant solubility and chemical homogeneity in TiO2 nanoparticles through sol-gel versus pechini syntheses, Inorg. Chem. 57 (2018) 7279–7289, https://doi.org/10.1021/acs.inorgchem.8b00926.

[15] F. Achouri, S. Corbel, L. Balan, K. Mozet, E. Girot, G. Medjahdi, M. Ben Said, A. Ghrabi, R. Schneider, Porous Mn-doped ZnO nanoparticles for enhanced solar and visible light photocatalysis, Mater. Des. 101 (2016) 309–316, https://doi.org/10.1016/j.matdes.2016.04.015.

[16] C.V. Reddy, I.N. Reddy, B. Akkinepally, V.V.N. Harish, K.R. Reddy, S. Jaesool, Mn-doped ZrO2 nanoparticles prepared by a template-free method for electrochemical energy storage and abatement of dye degradation, Ceram. Int. 45 (2019) 15298–15306, https://doi.org/10.1016/j.ceramint.2019.05.020.

[17] B. Bharati, N.C. Mishra, A.S.K. Sinha, C. Rath, Unusual structural transformation and photocatalytic activity of Mn doped TiO2 nanoparticles under sunlight, Mater. Res. Bull. 123 (2020), https://doi.org/10.1016/j.materresbull.2019.110710.

[18] B. Choudhury, S. Paul, G.A. Ahmed, A. Choudhury, Adverse effect of Mn doping on the magnetic ordering in Mn doped TiO 2 nanoparticles, Mater. Res. Express 2 (2015), https://doi.org/10.1088/2053-1591/2/9/096104.

[19] Q.R. Deng, X.H. Xia, M.L. Guo, Y. Gao, G. Shao, Mn-doped TiO2 nanopowders with remarkable visible light photocatalytic activity, Mater. Lett. 65 (2011) 2051–2054, https://doi.org/10.1016/j.matlet.2011.04.010.

[20] Y. Shu, J. Ji, Y. Xu, J. Deng, H. Huang, M. He, D.Y.C. Leung, M. Wu, S. Liu, S. Liu, G. Liu, R. Xie, Q. Feng, Y. Zhan, R. Fang, X. Ye, Promotional role of Mn doping on

[21] M.M. Islam, T. Bredow, Rutile band-gap states induced by doping with manganese in various oxidation states, J. Phys. Chem. C 119 (2015) 5534–5541, https://doi.org/10.1021/acs.jpcc.5b00023.

[22] A. Pérez-larios, A. Hernández-gordillo, G. Morales-mendoza, Enhancing the H 2 evolution from water – methanol solution using photocatalysts, Catal. Today 266 (2016) 9–16, https://doi.org/10.1016/j.cattod.2015.12.029.

[23] B. Srikanth, R. Goutham, R. Badri Narayan, A. Ramprasath, K.P. Gopinath, A. R. Sankaranarayanan, Recent advancements in supporting materials for immobilised photocatalytic applications in waste water treatment, J. Environ. Manage. 200 (2017) 60–78, https://doi.org/10.1016/j.jenvman.2017.05.063.

[24] M. Ge, J. Cai, J. Iocozzia, C. Cao, J. Huang, X. Zhang, J. Shen, S. Wang, S. Zhang, K. Q. Zhang, Y. Lai, Z. Lin, A review of TiO2 nanostructured catalysts for sustainable H2 generation, Int. J. Hydrogen Energy 42 (2017) 8418–8449, https://doi.org/10.1016/j.ijhydene.2016.12.052.

[25] D. Lu, P. Fang, X. Liu, S. Zhai, C. Li, X. Zhao, J. Ding, R. Xiong, A facile one-pot synthesis of TiO<inf>2</inf>-based nanosheets loaded with Mn<inf>x</inf>O<inf>y</inf> nanoparticles with enhanced visible light-driven photocatalytic performance for removal of Cr(VI) or RhB, Appl. Catal. B Environ. 179 (2015) 558–573, https://doi.org/10.1016/j.apcatb.2015.05.059.

[26] B.S. Pinheiro, L.L. Gimenes, A.J. Moreira, A.F. de Araújo, C.D. Freschi, G.P. G. Freschi, Speciation of As in environmental samples using the nano-TiO<inf>2</inf>/PCHG-FAAS online system, J. Environ. Sci. Heal. - Part A Toxic/Hazard. Subst. Environ. Eng. 52 (2017), https://doi.org/10.1080/10934529.2017.1340749.

[27] L.F.C. Gouvêa, A.J. Moreira, C.D. Freschi, G.P.G. Freschi, Speciation of nitrite, nitrate and p-nitrophenol by photochemical vapor generation of NO using High-Resolution Continuum Source Molecular Absorption Spectrometry, J. Food Compos. Anal. 70 (2018), https://doi.org/10.1016/j.jfca.2018.04.003.

[28] C.M. Lee, P. Palaniandy, I. Dahlan, Pharmaceutical residues in aquatic environment and water remediation by TiO2 heterogeneous photocatalysis: a review, Environ. Earth Sci. 76 (2017), https://doi.org/10.1007/s12665-017-6924-y.

[29] G. Pedroza-Herrera, I.E. Medina-Ramírez, J.A. Lozano-Álvarez, S.E. Rodil, Evaluation of the photocatalytic activity of copper doped TiO2 nanoparticles for the purification and/or disinfection of industrial effluents, Catal. Today (2018), https://doi.org/10.1016/j.cattod.2018.09.017.

[30] K. Esquivel, R. Nava, A. Zamudio-Méndez, M.V. González, O.E. Jaime-Acuña, L. Escobar-Alarcón, J.M. Peralta-Hernández, B. Pawelec, J.L.G. Fierro, Microwave-assisted synthesis of (S)Fe/TiO2 systems: effects of synthesis conditions and dopant concentration on photoactivity, Appl. Catal. B Environ. 140–141 (2013) 213–224, https://doi.org/10.1016/j.apcatb.2013.03.047.

[31] Y. Zhao, Z. Huang, W. Chang, C. Wei, X. Feng, L. Ma, X. Qi, Z. Li, Microwave-assisted solvothermal synthesis of hierarchical TiO2 microspheres for efficient electro-field-assisted-photocatalytic removal of tributyltin in tannery wastewater, Chemosphere 179 (2017) 75–83, https://doi.org/10.1016/j.chemosphere.2017.03.084.

[32] A.N. Kadam, R.S. Dhabbe, M.R. Kokate, Y.B. Gaikwad, K.M. Garadkar, Preparation of N doped TiO2 via microwave-assisted method and its photocatalytic activity for degradation of Malathion, Spectrochim. Acta - Part A Mol. Biomol. Spectrosc. 133 (2014) 669–676, https://doi.org/10.1016/j.saa.2014.06.020.

[33] V. Binas, V. Stefanopoulos, G. Kiriakidis, P. Papagiannakopoulos, Photocatalytic oxidation of gaseous benzene, toluene and xylene under UV and visible irradiation over Mn-doped TiO2 nanoparticles, J. Mater. 5 (2019) 56–65, https://doi.org/10.1016/j.jmat.2018.12.003.

[34] K. Umar, M.N.M. Ibrahim, A. Ahmad, M. Rafatullah, Synthesis of Mn-doped TiO2 by novel route and photocatalytic mineralization/intermediate studies of organic pollutants, Res. Chem. Intermed. 45 (2019) 2927–2945, https://doi.org/10.1007/s11164-019-03771-x.

[35] Z. Chen, Y. Li, M. Guo, F. Xu, P. Wang, Y. Du, P. Na, One-pot synthesis of Mn-doped TiO2 grown on graphene and the mechanism for removal of Cr(VI) and Cr(III), J. Hazard. Mater. 310 (2016) 188–198, https://doi.org/10.1016/j.jhazmat.2016.02.034.

[36] A.E. Shalan, M.M. Rashad, Incorporation of Mn 2+ and Co 2+ to TiO 2 nanoparticles and the performance of dye-sensitized solar cells, Appl. Surf. Sci. 283 (2013) 975–981, https://doi.org/10.1016/j.apsusc.2013.07.055.

[37] Z.P. Tshabalala, K. Shingange, F.R. Cummings, O.M. Ntwaeaborwa, G.H. Mhlongo, D.E. Motaung, Ultra-sensitive and selective NH3 room temperature gas sensing induced by manganese-doped titanium dioxide nanoparticles, J. Colloid Interface Sci. 504 (2017) 371–386, https://doi.org/10.1016/j.jcis.2017.05.061.

[38] A.R.R. Péry, M. Gust, B. Vollat, R. Mons, M. Ramil, G. Fink, T. Ternes, J. Garric, Fluoxetine effects assessment on the life cycle of aquatic invertebrates, Chemosphere 73 (2008) 300–304, https://doi.org/10.1016/j.chemosphere.2008.06.029.

[39] M. Saaristo, A. McLennan, C.P. Johnstone, B.O. Clarke, B.B.M. Wong, Impacts of the antidepressant fluoxetine on the anti-predator behaviours of wild guppies (Poecilia reticulata), Aquat. Toxicol. 183 (2017) 38–45, https://doi.org/10.1016/j.aquatox.2016.12.007.

[40] A.J. Moreira, A.C. Borges, B.B. de Souza, L.R. Barbosa, V.R. de Mendonça, C. D. Freschi, G.P.G. Freschi, Microwave discharge electrodeless mercury lamp (Hg-MDEL): an energetic, mechanistic and kinetic approach to the degradation of Prozac®, J. Environ. Chem. Eng. 7 (2019) https://doi.org/10.1016/j.jece.2019.102916, 102916.

[41] Y. Zhao, G. Yu, S. Chen, S. Zhang, B. Wang, J. Huang, S. Deng, Y. Wang, Ozonation of antidepressant fluoxetine and its metabolite product norfluoxetine: kinetics, intermediates and toxicity, Chem. Eng. J. 316 (2017) 951–963, https://doi.org/10.1016/j.cej.2017.02.032.

[42] M.S. Kostich, A.L. Batt, J.M. Lazorchak, Concentrations of prioritized pharmaceuticals in effluents from 50 large wastewater treatment plants in the US and implications for risk estimation, Environ. Pollut. 184 (2014) 354–359, https://doi.org/10.1016/j.envpol.2013.09.013.

[43] L. Yin, R. Ma, B. Wang, H. Yuan, G. Yu, The degradation and persistence of five pharmaceuticals in an artificial climate incubator during a one year period, RSC Adv. 7 (2017) 8280–8287, https://doi.org/10.1039/c6ra28351a.

[44] A. Moreira, A. Borges, B. de Sousa, V. de Mendonça, C. Freschi, G. Freschi, Photodegradation of fluoxetine applying different photolytic reactors: evaluation of the process efficiency and mechanism, J. Braz. Chem. Soc. 30 (2018) 1010–1024, https://doi.org/10.21577/0103-5053.20180250.

[45] C. Salazar, C. Ridruejo, E. Brillas, J. Yáñez, H.D. Mansilla, I. Sirés, Abatement of the fluorinated antidepressant fluoxetine (Prozac) and its reaction by-products by electrochemical advanced methods, Appl. Catal. B Environ. 203 (2017) 189–198, https://doi.org/10.1016/j.apcatb.2016.10.026.

[46] C. Wang, J. Niu, L. Yin, J. Huang, L.A. Hou, Electrochemical degradation of fluoxetine on nanotube array intercalated anode with enhanced electronic transport and hydroxyl radical production, Chem. Eng. J. 346 (2018) 662–671, https://doi.org/10.1016/j.cej.2018.03.159.

[47] H.S. Harned, C. Calmon, The properties of electrolytes in mixtures of water and organic solvents. I. Hydrochloric acid in ethanol- and isopropanol-water mixtures of high dielectric constant, J. Am. Chem. Soc. 61 (1939) 1491–1494, https://doi.org/10.1021/ja01875a047.

[48] F.T.L. Muniz, M.A.R. Miranda, C. Morilla Dos Santos, J.M. Sasaki, The Scherrer equation and the dynamical theory of X-ray diffraction, Acta Crystallogr. Sect. A Found. Adv. 72 (2016) 385–390, https://doi.org/10.1107/S205327331600365X.

[49] G. Louit, S. Foley, J. Cabillic, H. Coffigny, F. Taran, A. Valleix, J.P. Renault, S. Pin, The reaction of coumarin with the OH radical revisited: hydroxylation product analysis determined by fluorescence and chromatography, Radiat. Phys. Chem. 72 (2005) 119–124, https://doi.org/10.1016/j.radphyschem.2004.09.007.

[50] J. Zhang, Y. Nosaka, Quantitative detection of OH radicals for investigating the reaction mechanism of various visible-light TiO2 photocatalysts in aqueous suspension, J. Phys. Chem. C 117 (2013) 1383–1391, https://doi.org/10.1021/jp3105166.

[51] E.S. Papas, C.N. Chaldezos, J. Atta-Politou, M.A. Koupparis, Construction of a fluoxetine ion chemical sensor and its application for the determination of pKa value of fluoxetine conjugated acid, complexation study with β-cyclodextrin and

[52] formulations assay, Anal. Lett. 43 (2010) 2171–2183, https://doi.org/10.1080/00032711003687104.

[52] P. Umek, C. Bittencourt, P. Guttmann, A. Gloter, S.D. Skapin, D. Arcon, Subscriber Access Provided by BEIJING UNIV Mn 2+ Substitutional Doping of TiO 2 Nanoribbons: A Three-Step Approach, 2014, https://doi.org/10.1021/jp5063989.

[53] D.O. Adekoya, M. Tahir, N.A.S. Amin, g-C3N4/(Cu/TiO2) nanocomposite for enhanced photoreduction of CO2 to CH3OH and HCOOH under UV/visible light, J. CO2 Util. 18 (2017) 261–274, https://doi.org/10.1016/j.jcou.2017.02.004.

[54] Y. Dai, H. Jiang, Y. Hu, C. Li, Hydrothermal synthesis of hollow Mn2O3 nanocones as anode material for Li-ion batteries, RSC Adv. 3 (2013) 19778–19781, https://doi.org/10.1039/c3ra42664e.

[55] S. Jaiswar, K.D. Mandal, Evidence of enhanced oxygen vacancy defects inducing ferromagnetism in multiferroic CaMn7O12 manganite with sintering time, J. Phys. Chem. C 121 (2017) 19586–19601, https://doi.org/10.1021/acs.jpcc.7b05415.

[56] N.T.T. Truc, D.S. Duc, D. Van Thuan, T. Al Tahtamouni, T.-D. Pham, N.T. Hanh, D.T. Tran, M.V. Nguyen, N.M. Dang, N.T.P. Le Chi, V.N. Nguyen, The advanced photocatalytic degradation of atrazine by direct Z-scheme Cu doped ZnO/g-C3N4, Appl. Surf. Sci. 489 (2019) 875–882, https://doi.org/10.1016/j.apsusc.2019.05.360.

[57] M. Payá, B. Halliwell, J.R.S. Hoult, Interactions of a series of coumarins with reactive oxygen species, Biochem. Pharmacol. 44 (1992) 205–214, https://doi.org/10.1016/0006-2952(92)90002-z.

[58] P. Raizada, S. Sharma, A. Kumar, P. Singh, A.A. Parwaz Khan, A.M. Asiri, Performance improvement strategies of CuWO4 photocatalyst for hydrogen generation and pollutant degradation, J. Environ. Chem. Eng. 8 (2020), https://doi.org/10.1016/j.jece.2020.104230, 104230.

[59] J. Treml, K. Šmejkal, Flavonoids as potent scavengers of hydroxyl radicals, Compr. Rev. Food Sci. Food Saf. 15 (2016) 720–738, https://doi.org/10.1111/1541-4337.12204.

[60] W.L. Silva, M.A. Lansarin, P.R. Livotto, J.H.Z. dos Santos, Photocatalytic degradation of drugs by supported titania-based catalysts produced from petrochemical plant residue, Powder Technol. 279 (2015) 166–172, https://doi.org/10.1016/j.powtec.2015.03.045.

[61] A. Hu, X. Zhang, D. Luong, K.D. Oakes, M.R. Servos, R. Liang, S. Kurdi, P. Peng, Y. Zhou, Adsorption and photocatalytic degradation kinetics of pharmaceuticals by TiO2 nanowires during water treatment, Waste Biomass Valorization 3 (2012) 443–449, https://doi.org/10.1007/s12649-012-9142-6.

[62] E. Márquez Brazón, C. Piccirillo, I.S. Moreira, P.M.L. Castro, Photodegradation of pharmaceutical persistent pollutants using hydroxyapatite-based materials, J. Environ. Manage. 182 (2016) 486–495, https://doi.org/10.1016/j.jenvman.2016.08.005.